









ARTICLE

<https://doi.org/10.1038/s41467-019-09213-x>

OPEN

The operational environment and rotational acceleration of asteroid (101955) Bennu from OSIRIS-REx observations

C.W. Hergenrother¹, C.K. Maleszewski¹, M.C. Nolan¹ , J.-Y. Li² , C.Y. Drouet d'Aubigny¹, F.C. Shelly¹, E.S. Howell¹, T.R. Kareta¹ , M.R.M. Izawa³, M.A. Barucci⁴ , E.B. Bierhaus⁵, H. Campins⁶, S.R. Chesley⁷, B.E. Clark⁸ , E.J. Christensen¹, D.N. DellaGiustina¹, S. Fornasier⁴ , D.R. Golish¹ , C.M. Hartzell⁹, B. Rizk¹, D.J. Scheeres¹⁰, P.H. Smith¹, X.-D. Zou², D.S. Lauretta¹  & The OSIRIS-REx Team

During its approach to asteroid (101955) Bennu, NASA's Origins, Spectral Interpretation, Resource Identification, and Security-Regolith Explorer (OSIRIS-REx) spacecraft surveyed Bennu's immediate environment, photometric properties, and rotation state. Discovery of a dusty environment, a natural satellite, or unexpected asteroid characteristics would have had consequences for the mission's safety and observation strategy. Here we show that spacecraft observations during this period were highly sensitive to satellites (sub-meter scale) but reveal none, although later navigational images indicate that further investigation is needed. We constrain average dust production in September 2018 from Bennu's surface to an upper limit of 150 g s^{-1} averaged over 34 min. Bennu's disk-integrated photometric phase function validates measurements from the pre-encounter astronomical campaign. We demonstrate that Bennu's rotation rate is accelerating continuously at $3.63 \pm 0.52 \times 10^{-6}$ degrees day⁻², likely due to the Yarkovsky-O'Keefe-Radzievskii-Paddack (YORP) effect, with evolutionary implications.

¹Lunar and Planetary Laboratory, University of Arizona, Tucson, AZ, USA. ²Planetary Science Institute, Tucson, AZ, USA. ³Institute for Planetary Materials, Okayama University-Misasa, Misasa, Tottori, Japan. ⁴LESIA, Observatoire de Paris, Université PSL, CNRS, Sorbonne Université, Univ. Paris Diderot, Sorbonne Paris Cité, Meudon, France. ⁵Lockheed Martin Space, Littleton, CO, USA. ⁶Department of Physics, University of Central Florida, Orlando, FL, USA. ⁷Jet Propulsion Laboratory, California Institute of Technology, Pasadena, CA, USA. ⁸Department of Physics and Astronomy, Ithaca College, Ithaca, NY, USA. ⁹Department of Aerospace Engineering, University of Maryland, College Park, MD, USA. ¹⁰Smead Department of Aerospace Engineering, University of Colorado, Boulder, CO, USA. A full list of authors and their affiliations appears at the end of the paper. Correspondence and requests for materials should be addressed to C.W.H. (email: chergen@orex.lpl.arizona.edu).

The Approach phase for the OSIRIS-REx mission occurred between 17 August 2018 and 2 December 2018¹. Observations of near-Earth asteroid (NEA) Bennu began as the asteroid was just bright enough for detection by the OSIRIS-REx Camera Suite (OCAMS)². The three goals for the Approach phase of the mission were to optically acquire the asteroid, survey the vicinity of the asteroid for any hazards (natural satellites or dust trails) that may be present, and characterize the asteroid point-source properties for comparison with ground- and space-based telescopic data^{1,3}. Here we show that we detect no hazards within the sub-meter sensitivity limits of our Approach phase observations. Further work will follow since images from our navigation camera later revealed the existence of apparent particles in close vicinity of Bennu⁴. We find strong agreement between the pre-encounter and OSIRIS-REx disk-integrated photometric properties. We detect a continuous acceleration in Bennu's rotation and conclude that it results from the YORP effect⁵.

Results

Search for dust. The first dedicated science observation of Bennu by OSIRIS-REx was a search for dust on 11 and 12 September 2018 when Bennu was at a heliocentric distance of 1.21 au. We used the OCAMS PolyCam and MapCam instruments² to survey all space within a 35,000 km radius of Bennu. If present, unbound dust released due to outgassing processes would appear as diffuse cometary features (trails or tails) along the directions between the anti-solar and anti-heliocentric velocity vectors⁶. The shape of such features is governed by the balance between radiation pressure and gravity and is particle size-dependent. Only particles ejected in the anti-solar direction two to eight weeks prior to the observations would have been detected in our MapCam images. We observed no detectable dust during this search.

We determined upper limits of 300 kg for the dust mass within 405 km of Bennu and 150 g s^{-1} averaged over 34 min for the average dust production rate by considering the properties and ephemeris of Bennu, assuming a dust flux such as that from a near-surface coma, and assuming the dust ejection velocity measured for comet 67 P at perihelion (see methods). Observations in the thermal infrared taken with the Spitzer space telescope (hereafter, Spitzer) yielded upper limits on dust mass from Bennu of 1000 kg and on dust production rate of 1 g s^{-1} (ref. 7). The OSIRIS-REx Approach phase dust searches were comparable in sensitivity to Spitzer observations with regards to dust mass but much less sensitive to lower dust production rates.

Our upper limit on Bennu's average dust production rate is on the extreme lower end of those of main belt comets, which are in the range of 100 to 4000 g s^{-1} (ref. 8). Asteroid (3200) Phaethon, the parent of the Geminid meteor shower, reaches a peak dust production of approximately 300 g s^{-1} , (ref. 9) during its perihelion passage, possibly driven by thermal desiccation of surface rocks. As Bennu's surface has many rocks with apparent fracturing that may have been thermally induced^{10,11} similar dust production due to thermal desiccation may occur on Bennu.

We will conduct two dedicated searches for dust mass loss at a high phase angle of approximately 130 degrees during the Detailed Survey phase of the mission in spring 2019¹. The higher phase angle of these searches enhances dust observability if the dust particles are forward-scattering, as would be expected for sub-micron-sized particles¹².

Search for natural satellites. The fraction of NEAs larger than 300 m with satellites is $15 \pm 4\%$ ¹³. The smallest asteroid satellite yet observed is approximately 44 m in diameter, around the primary body NEA 2000 CO₁₀₁¹⁴. Pre-encounter modeling suggests that any Bennu satellites with diameters larger than 1 m

could be stable on orbits within 20 km, and diameters of 10 cm could be stable on orbits within 12 km^{15,16}. Ground-based radar observations were sensitive to satellites of Bennu down to a size of 2 to 20 m diameter, depending on the rotation rate of the satellites¹⁷.

For OSIRIS-REx, we calculated the detectable satellite size using the lower-limit bound of Bennu's albedo (0.03) and the upper-limit on steepness of the phase function slope (0.043 mag per degree) determined from the ground¹⁸. We tested different exposure durations to decrease the glare of Bennu and allow detections down to a projected height of 20 m above the sunlit limb. From the multiple search dates, the cadence of images taken per date, and multiple search methods—including visual inspection and use of the asteroid-hunting Catalina Sky Survey automated moving object detection software¹⁹—we estimated that our detection efficiency would be approximately 99% for satellites 10 cm and larger. Orbiting satellites would spend some fraction of their orbits in front of or behind the asteroid. The multiple dates and 5-h observing windows per date ensured that orbiting objects were detectable.

We conducted our search for natural satellites using PolyCam (Fig. 1). Initially, when the spacecraft was at a range of 3100 km, the search was over an area of 60 km radius when our observations were sensitive to 0.5 m or larger satellites. Later, as the spacecraft got closer, satellites as small as 8 cm would have been bright enough to be imaged within 18 km of Bennu. As the spacecraft approached Bennu, the PolyCam field of view narrowed down to smaller areas of the sky, allowing us to search for smaller satellites (Fig. 2). In all, we used PolyCam and MapCam on ten dates to search for satellites, and our observations were sensitive to objects as small as 24 cm in diameter within the entire Hill Sphere (31 km)²⁰ (Supplementary Table 1).

The Hayabusa mission could detect satellites down to 1 m around NEA (25143) Itokawa²¹, the Rosetta mission could detect satellites between 1 and 6 m around comet 67 P²², and the Dawn mission could detect satellites as small as 3 m around (4) Vesta and 12 m around (1) Ceres^{23,24}. In contrast, the high sensitivity of our OCAMS instruments allowed us to search for satellites at the sub-meter scale. No satellites were detected down to our sensitivity limits.

Although we detected no dust or satellites during our dedicated search with the OCAMS instruments during the Approach phase, images collected in January 2019 by one of the navigation cameras (NavCam1)²⁵ have since revealed apparent particles in the vicinity of Bennu⁴. These probable particles are likely to be smaller than the sensitivity limit of the Approach-phase satellite search. Their nature and production mechanism are still under investigation, although they appear to originate from Bennu. We plan to continue monitoring the near-Bennu environment throughout the rest of the mission.

Disk-integrated phase function. From the ground, the disk-integrated phase function of Bennu was determined using measurements obtained between 2005 and 2012¹⁸. For direct comparison to the ground-based data, we first limited the OCAMS data to the same phase angle range as the ground-based data. This analysis yields a linear fit with $H_V = 20.51 \pm 0.04$ and $B_V = 0.039 \pm 0.001$, in good agreement with the ground-based data. The phase slope of Bennu is similar to that of other low-albedo main belt asteroids such as the C, F, and P types (0.04 to 0.05 mag per degree of phase angle)²⁶.

We then modeled the full disk-integrated phase dependence of Bennu with several methods, including the Lommel-Seeliger model²⁷, the IAU H-G model²⁸, and the more recently adopted

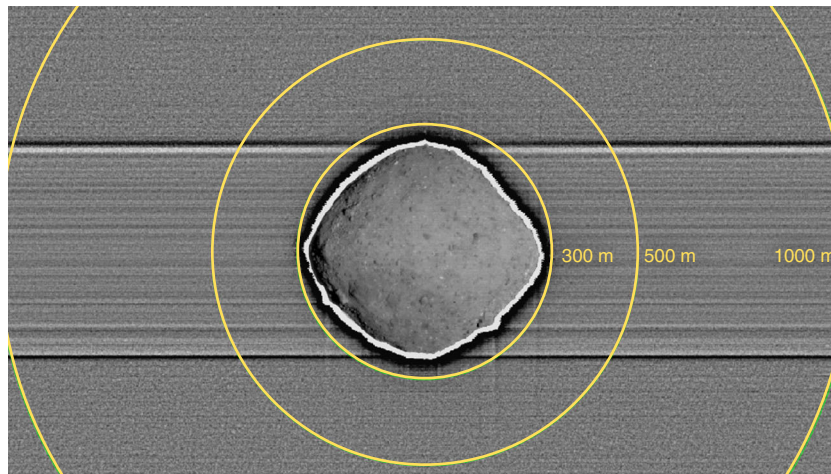


Fig. 1 Satellite-search imaging of the near-asteroid region. The image is a median combination of 15 PolyCam exposures from 10 November 2018 tracking the motion of the asteroid. This method enhances the relative detectability of satellites while suppressing the signal of stars and other background astronomical objects. The yellow circles denote distances from the Bennu center of figure. The horizontal features are due to charge smear. No satellites are apparent

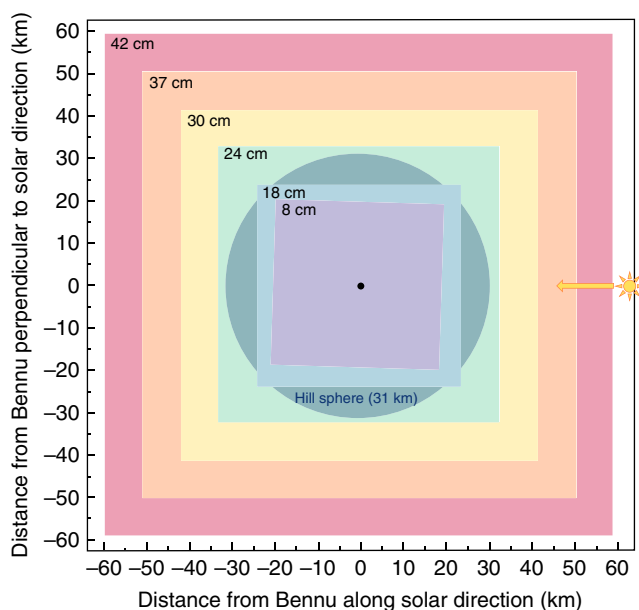


Fig. 2 Schematic illustrating visibility of detectable natural satellites. The minimum detectable diameter is given within the upper left corner of each search region. Bennu is marked at the center of the figure. Also marked is the Hill Sphere, or the region in which objects remain in orbit due to Bennu's gravity. We completed an extensive search for natural satellites that sampled the entire Hill Sphere with a sensitivity to 24 cm satellite diameter. We detected none at this sensitivity level. Source data are provided in Supplementary Table 1

H, G_1, G_2 and H, G_{12} models^{29,30} (see Methods) (Fig. 3). For each model, the parameter H is the absolute magnitude. Each particular value of G helps define the curve shapes of each model. The IAU H - G model fails to correctly reproduce the data at very small phase angles, as it predicts a larger opposition effect than is present. Difficulty modeling the opposition effect of low-albedo objects is a recognized deficiency of this model³¹. The H, G_1, G_2 model results in an artificial drop in the magnitude at phase angles $< 1^\circ$. We fitted the v-band phase function data of Bennu with both the original and the revised H, G_{12} models^{29,30} (Supplementary Table 2). The revised H, G_{12} model fits the data

in the full range of phase angles that they cover (Fig. 3). In general, the G -parameters (G, G_1, G_2 , and G_{12}) of all three models suggest a shallower phase slope with increasing wavelength, consistent with phase reddening in the visible wavelengths¹⁰.

The disk-integrated Lommel-Seeliger model yields a geometric albedo of 0.044 ± 0.002 and Bond albedo of 0.0170. The H, G_{12} model found an H_v of 20.41 ± 0.02 . This compares well with the best pre-encounter H_v value of $20.56^{+0.05}_{-0.15}$ ¹⁸. The ground-based photometry did not include observations at phase angles less than 15 degrees phase angle but did extend up to 100 degrees phase angle. The good agreement between the ground-based and OSIRIS-REx photometric results highlights the importance of supporting ground-based asteroid observations at multiple observing geometries.

Comparing the magnitude derived from the linear fit (i.e. excluding the opposition effect) with the absolute magnitude from the revised H, G_{12} model, we found a magnitude increase (Δm) of 0.20 mag that could be related to the opposition effect (Fig. 3, inset). The parameters of Bennu's opposition effect are consistent with the values reported in the literature for about 40% of low-albedo asteroids with average opposition effect amplitudes of 0.16 ± 0.05 mag and starting phase angles of 6 to 7 degrees^{32,33}.

Rotation state. We had extensive knowledge of the rotation state of Bennu from our pre-encounter astronomical campaign^{3,17,18} when lightcurve observations yielded a synodic rotation period of 4.2905 ± 0.0065 h¹⁸. The observed low amplitude and trimodal (three maxima and three minima) lightcurve was consistent with the rotation of a nearly spherical body observed at high phase angles. We used the best-fit shape and pole position for Bennu from a combination of radar images and lightcurve data¹⁷. The sidereal rotation period determined from the lightcurve and radar data was 4.29746 ± 0.002 h. Bennu's obliquity was determined to be 178 ± 4 degrees with the rotation pole at $(87, -65) \pm 4$ degrees (J2000 equatorial coordinates)¹⁷. From ground-based and Hubble Space Telescope observations in 1999, 2005, and 2012, an increase was detected in the rotation rate of Bennu of $2.64 \pm 1.05 \times 10^{-6}$ degrees day⁻², possibly due to YORP thermal torques³⁴.

For the present study, we measured Bennu's rotation rate by obtaining a series of asteroid light curves using the OCAMS MapCam instrument with the b', v, w, and x spectral filters (centered at 470, 550, 770, and 860 nm wavelengths, respectively)¹.

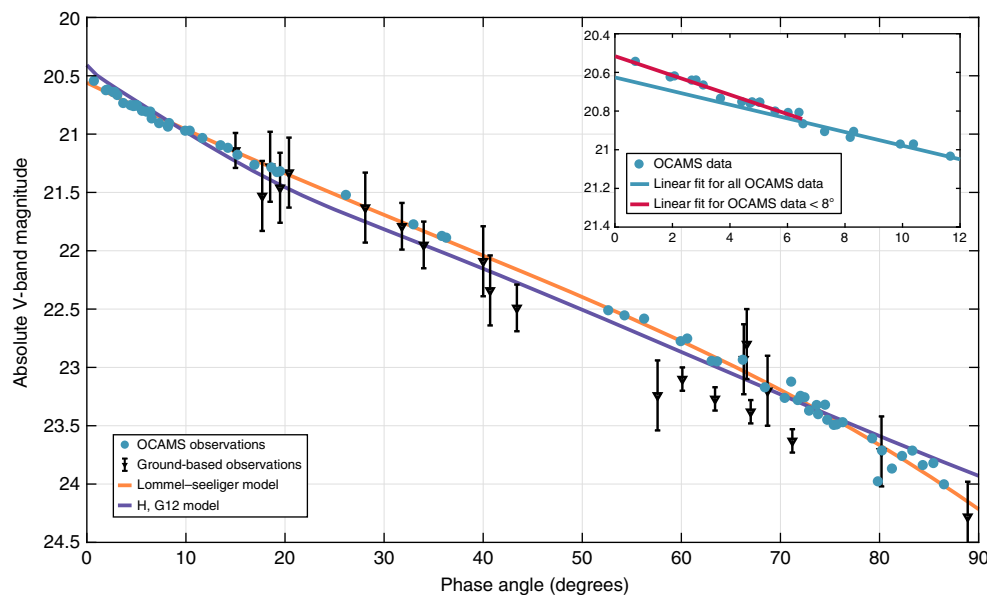


Fig. 3 Phase function observations and models for Benu. Over-plotted are the model fits to the new data: a Lommel-Seeliger model and a revised H,G_{12} model. The ground-based measurements are published in¹⁸. We originally converted the ground-based measurements to the v-band magnitude scale, plotted with 1-sigma photometric error bars. The 1-sigma photometric error bars for OCAMS data are less than or equal to the size of the data points. Inset, upper right: The OSIRIS-REx measurements at low phase angles (0 to 12 degrees). We plot this subset of the data to illustrate the small opposition effect present for asteroid Benu. The small opposition effect is consistent with what we would expect for low-albedo, carbonaceous bodies. The red line is the linear fit to observations made at less than 7.5 degrees phase angle. The blue line is the linear fit to all OSIRIS-REx data points at greater than 7.5 degrees phase angle. Source data are provided in Supplementary Tables 2 and 3

The OSIRIS-REx lightcurves have a different shape than the ground-based lightcurves, with four peaks instead of three, due to the Approach phase data being taken at much lower solar phase angle (4 to 18 degrees) than any of the earlier telescopic data (60 to 71 degrees).

Benu's rotation rate has accelerated since 1999, but previous work could not distinguish between continuous spin-up due to YORP and a step change in rotation rate due to a change in moment of inertia³⁴. Here we confirm that the acceleration has continued to the present day and is most likely due to the YORP effect. We derive an acceleration of $3.63 \pm 0.52 \times 10^{-6}$ degrees day⁻², with a rotation rate of 2011.1697 ± 0.0011 degrees day⁻¹, and a period of 4.296007 ± 0.000002 h (compared to a rotation rate of 2011.1445 ± 0.0011 degrees day⁻¹ and period of 4.296061 ± 0.000002 h at the J2000 epoch). Figure 4 shows the OSIRIS-REx Approach phase lightcurve and model fits using the shape model and this acceleration (black curve). The acceleration that we determine is a better fit to the observations than the previously determined value³⁴ (Fig. 4, orange curve) or a constant rotation rate since 2009 (Fig. 4, green curve). The inset plot shows that the rotational phase determined at four epochs is consistent with a rotation rate increasing along a quadratic curve. This is evidence for a continuous change—i.e., YORP—not a step change.

The doubling time for this acceleration is about 1.5 million years, indicating that Benu's surface could be unstable on million-year timescales. However, such timescales are much shorter than Benu's apparent surface age of at least 100 million years^{10,20} suggesting that the YORP acceleration has changed over time, possibly due to changes in Benu's orbit or its shape³⁵. All of the NEAs, including Benu, for which YORP has been detected have been accelerating³⁶, and many of the top-shaped NEAs are binary systems; perhaps Benu will evolve to this state. The OSIRIS-REx spacecraft will continue to probe the near-surface environment of Benu to resolve the relationship between its surface and its rotation state.

Methods

Search for dust near Benu. A sequence of images centered on Benu was obtained using the OCAMS PolyCam and MapCam imagers. The image sequence was median co-added on the motion of Benu to produce a map of the dust near Benu. Dust would have exhibited itself as diffuse features either around Benu, trailing Benu in the anti-solar direction, or trailing Benu along its orbit.

PolyCam dust plume search images were collected on 11 September 2018 when Benu was at a range of 1.05 million km and phase angle of 43 degrees. The MapCam images were collected on the following date when Benu was at a range of 1.00 million km and phase angle of 44 degrees. On these dates, PolyCam covered a region of Benu's orbit extending 7300 km leading and trailing Benu. MapCam covered a region along Benu's orbit that extends 35,000 km leading and trailing Benu.

The 11 and 12 September dates were chosen because Benu's apparent position in J2000 celestial coordinates placed it in a part of the Milky Way that is relatively less dense in stars. From the beginning of the Approach phase to the time of the spacecraft's second asteroid approach maneuver (15 October), Benu traversed a very dense part of the Milky Way as seen from the spacecraft. Although none of the dates were optimal, 11 and 12 September were the best available while also maximizing the region of space around Benu that was searched for dust.

Modeling of possible dust trails for Benu. The model of ref. ⁶ was implemented to model potential dust trails from Benu. We use an adapted version of the code originally developed by Jean-Baptiste Vincent³⁷. The Vincent version of the model uses numerical integration to track the position and velocity of a dust particle that is ejected from the surface of the parent body. This is opposed to the analytical equations first proposed in ref. ⁶. Most of the adaptations we made involve changing the location of observing from Earth to the spacecraft's position. This allowed us to generate trail locations as a function of right ascension and declination.

For simplicity, we assumed constant particle sizes as a function of beta as opposed to implementing a particle size distribution found in other versions of this model. A particle size for a particular syndyne can be calculated from Eq. 3 in ref. ⁶. To estimate times in which the earliest particles ejected, trails from our model were plotted over the median co-added images of Benu from the hazards search. The combined plot was visually inspected to determine at what time each trail would leave the field-of-view of the co-added image. The range of particle sizes used to estimate ejection time are for beta values of 0.01 and 0.1. This corresponds to grain sizes of 66.1 and 3.3 microns respectively.

Determining the bound on the mass loss rate. To provide a bound on the mass loss rate of a detectable coma, we adapt a method³⁸ used for members of the

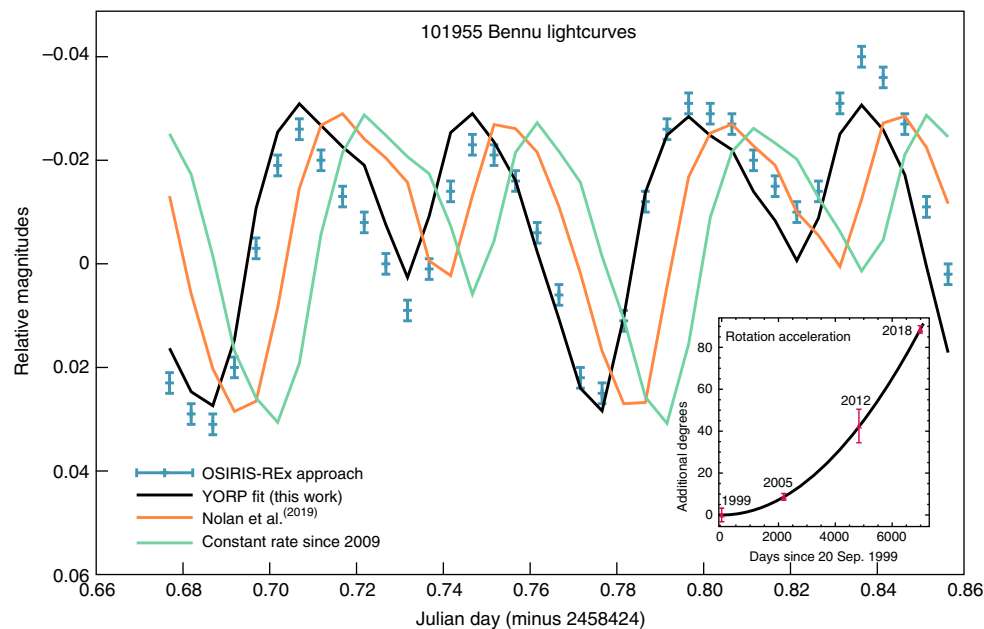


Fig. 4 Lightcurve data and models for Benu on 2 November 2018. The blue crosses are the OSIRIS-REx observations with their associated 1-sigma photometric uncertainties. The black curve (best fit to peaks and minima) shows the YORP acceleration determined from fitting the Approach phase observations with 1-sigma uncertainties. The orange lightcurve using the previously reported acceleration value³⁴ does not fit as well as the black curve. The green curve assumes a constant rotation rate since 2009. The inset plot shows the quadratic increase of rotation phase with time, consistent with rotational acceleration due to YORP. Source data are provided as a Source Data file

Centaur population. The goal of this method is to estimate the total mass of a possible coma from light measured using photometry of an annulus between two circular apertures. We also estimate the approximate time that dust would remain in the given annulus. Dividing these two quantities provides us with a mass loss rate.

A median co-add of images from the Dust Search campaign was created, and then two photometry measurements of Benu at radii of 20 and 30 arcseconds were measured. The IRAF phot package was used to determine instrumental magnitude of these apertures. We also corrected for sections of the point spread function leaking into the coma annulus as suggested in ref. ³⁸. These magnitudes were transformed into a R-band magnitude system where the apparent magnitude of the Sun is known (for Eq. 3).

Equations 1, 3, and A4 in ref. ³⁸ were used to calculate the bound mass in the annulus between the two photometric apertures. Phase angle, Benu-Sun distance, and Benu-OSIRIS-REx distances were calculated from Benu's ephemeris using JPL HORIZONS. The phase darkening correction was interpolated from the phase darkening curve developed in refs. ^{12,39}. To convert from cross-section to mass (equation A4), we assume that the R-band albedo is equal to the V-band albedo and set it to a value of 0.045. We assume the same particle sizes, $a_+ = 1$ cm and $a_- = 0.1$ micron^{38,40}.

The residence time is calculated from Eq. 4 in ref. ³⁸. We adopt an outflow velocity of 25 m s^{-1} , which is the estimated value of the ejection velocity for 67P/Churyumov-Gerasimenko at perihelion⁴¹. This value is chosen since the perihelion of 67P is close to the Benu-Sun distance during the hazards search (1.3 vs. 1.2 au). It also agrees with measurements taken of the ejection velocity from the Rosetta mission⁴².

Search for natural satellites around Benu. Dedicated searches for natural satellites in orbit around Benu were conducted on 10 separate dates. A summary of the observing circumstances and detection limits of each date is given in Supplementary Table 1. Observations were collected over the course of 5 h (between 4:00 and 9:00 UTC) on each date.

Each date of the search consisted of 3×3 mosaic fields with approximately 10% overlap between each field. Each field was imaged between 15 and 30 times over a span of time allowing an object with Benu rates of motion to move between 5 and 30 pixels relative to the background stars. This dwell time on each field ranged from 4.2 to 25.7 min depending on Benu's varying rates of relative motion. Each field was visited between 2 and 4 times on each date. As a result, each field was imaged 60 times per date. Exposure times ranged from 5 s to 0.15 s. Shorter exposure times were used during the later search dates to avoid saturation and pixel blooming near the asteroid. The shorter exposure times were set to still allow the detection of satellites as small as 10 cm.

On 23 to 28 October 2018, only PolyCam was used. Observations between 30 October and 11 November 2018 used a combination of MapCam and PolyCam.

Each post-30 October search consisted of a 3×3 MapCam mosaic and a single PolyCam field centered on Benu. The 30 and 31 October PolyCam fields were not used for satellite searching as Benu was located near the edge or outside the small PolyCam field-of-view due to the greater navigational uncertainty after the third asteroid approach maneuver.

Three different methods were utilized to search for satellites within the OCAMS images. The first involved manually blinking the 15 or 30 images taken per field per visit for moving objects. The second combined, or stack and shifted, all of the images taken during a visit on the motion of Benu. The combined images minimized the signal of background stars while enhancing the brightness of objects moving at the rate of Benu. The third search method used the moving object detection software of the Catalina Sky Survey (CSS) to automatically detect satellites¹⁹. The CSS software was used on 5 images at a time. Due to the large number (15–30) images taken per visit, up to 6 different combinations of the images were run through the CSS software enabling multiple opportunities for detection. The software approach was not used on 23–25 October due to the slow apparent motion of Benu and any satellites relative to the background stars. It was also not applicable on 30–31 October and 10–11 November due to the short exposure times used and the low number of detectable background stars.

The sensitivity and efficiency of the satellite search was improved by conducting a search for Earth Trojan Asteroids (ETAs) during the outbound cruise phase in February 2017^{43,44}. By exercising the entire moving object detection process, lessons learned during the ETAs search resulted in changes to detection software, number and cadence of observations, exposure times, and the use of both PolyCam and MapCam.

OCAMS disk-integrated photometry calibration. The combination of the OCAMS narrow point spread function (PSF) with its detector's strongly non-uniform pixel response makes photometric calibration using standard stars more challenging than expected. A dedicated calibration campaign has yielded valuable insights but disappointing results. A second campaign incorporating lessons learned from our first attempt is planned. In the interim, we use defocused images of open star cluster NGC 3532 to derive an absolute radiometric calibration for the PolyCam. We then use near simultaneous MapCam and PolyCam observations of Benu to transfer this calibration to the MapCam.

During outbound cruise, PolyCam acquired a through-focus sequence of images of NGC 3532. In one of these images, stars are defocused enough to cover approximately 100 pixels, thereby minimizing the effects of aliasing. We exclude stars near the edge of the detector or in pixel regions which do not behave like the bulk of the detector. Stars for which any raw counts are out of the linear range for PolyCam (<12,500 DN) are also rejected. Despite the significant defocus, stars are still well resolved and can be automatically detected, identified and measured. Stars close to each other are also excluded. Visual inspection of each of the remaining stars is used to exclude a further 95 stars with PSF indicative of one or more

unresolved companions, leaving 187 stars in our sample. In addition to being an open cluster, NGC 3532 is also a diffuse nebula, so we estimate and remove the local background of the nebula at each star.

Given the panchromatic filter's 650 nm center wavelength, the integrated star flux is then compared to the R magnitude reported by the American Association of Variable Star Observers (AAVSO) NGC 3532 Standard Field catalog. The fit between the logarithm of measured DN/s and the AAVSO Catalog m_R magnitudes is very good ($R = 0.998$). When corrected to the OSIRIS-REx reference temperature that fit is:

$$m_R = -2.5 \log_{10}(\text{DN}/s(\text{PolyCam } T_{\text{ref}})) + 18.2180 \quad (1)$$

By design all OCAMS panchromatic filters have identical bandpasses. This allows us to use Benu as a proxy to extend PolyCam's absolute calibration to the MapCam. To do this, we use a pair of PolyCam and MapCam images taken on 25 November 2018. Between the two images Benu rotated one full rotation plus 1 min and 47 s (2.5 degrees). As a result, Benu presents essentially the same face to the cameras in both images. We estimate how much this difference could affect our calibration, by comparing the integrated flux in PolyCam images taken 7 min before and 7 min after the one used to compare with MapCam. The integrated flux difference between those images is approximately 0.5%.

PolyCam and MapCam imaged Benu at slightly different phase angles ($\Delta\alpha = 0.4$ degrees). In the time between the two images the spacecraft also closed in on Benu by approximately 1.5 km. Correcting for these effects we estimate that the integrated flux observed by MapCam should be 1.4% greater than PolyCam's.

We use the OCAMS radiometrically calibrated frad product to integrate Benu's flux and relate the two cameras. This product is a dark subtracted, flat fielded, radiometrically calibrated (frad = DN/s/277,035). After correcting for phase angle and distance changes, the calculated ratio between the two cameras is 24.902 and the derived calibration is given by:

$$m_R = -2.5 \log_{10}(\text{MapCam.frad}_{\text{PAN}} \times 24.90 \times 277,035) + 18.2180 \quad (2)$$

Disk-integrated photometry modeling. The ground-based campaigns covered a range of phase angles from 15.0 to 95.6 degrees yielding an absolute magnitude (H_v) of 20.61 ± 0.20 and phase slope (B_v) of 0.040 ± 0.003 magnitude per degree of phase angle. We applied a known correlation between the slope of the linear phase function and the albedo of asteroids^{26,45} to estimate a global average geometric albedo of 0.030–0.045¹⁸ for Benu. For the spacecraft phase function campaign, we acquired images daily between 2 October and 2 December 2018. These observations yielded photometric measurements covering a phase angle range from 0.7 to 86.5 degrees in the MapCam v filter (Supplementary Table 2).

The disk-integrated Lommel-Seeliger phase function model (with an exponential phase function and a polynomial in the exponent)²⁷ is

$$\Phi(\alpha) = p \left[1 + \sin \frac{\alpha}{2} \tan \frac{\alpha}{2} \ln \left(\tan \frac{\alpha}{4} \right) \right] f(\alpha) \quad (3)$$

and

$$f(\alpha) = \exp(p_1\alpha + p_2\alpha^2 + p_3\alpha^3) \quad (4)$$

where α is phase angle in degrees; p is geometric albedo, and p_1 , p_2 , and p_3 are parameters that defines the shape of the phase function. Resulting parameters for the Lommel-Seeliger, as well as the IAU H,G , Muinonen H,G_1,G_2 and revised H,G_{12} models are given in Supplementary Table 2.

We fitted the v-band phase function data of Benu with both the original and the revised H, G_{12} models^{29,30}. We used the implementation of both H, G_{12} models in the photometry module of the Python package for small-body planetary astronomy sbpy that is currently under development⁴⁶. The non-linear fitting was performed with the Levenberg-Marquardt algorithm⁴⁷ as implemented in the fitting module in astropy, which is a community-developed core Python package for astronomy⁴⁸.

Rotation rate of Benu. We obtained photometric measurements over two full asteroid rotations (around 8.6 h). We used the integrated flux from MapCam images by adding up the radiance from all of the pixels on Benu to compute a lightcurve. We then compared these lightcurves with the predicted brightness using version 13 of the asteroid shape model³⁵ (Fig. 4).

To compute the rotational acceleration, we followed the procedure from³⁴, adding the data from these observations to the ground-based and Hubble Space Telescope observations from 1999, 2005, and 2012 as used in that work. We used the shape model from³⁵ along with the rotation pole from⁴⁹ and the observing geometry to compute synthetic lightcurve points using a Lommel-Seeliger photometric function for the observing times of the data. At each of the observation epochs, we adjusted the rotation phase of the model slightly to minimize chi-squared using the method of⁵⁰ for the data taken at that epoch. We took the absolute phase uncertainty at each of those epochs to be the amount of rotation required to increase reduced chi-squared by 1. The phase uncertainties at each epoch (3.2, 1.6, 8.0, and 1.8 degrees, respectively) are slightly larger than those reported in³⁴, probably because the shape model used in that analysis was determined in part from those same lightcurve data, while this work uses a shape

model from spacecraft imagery. There was no 2018 data point in the earlier analysis, as these data were not yet available.

Because the absolute rotation phase is known to within 10 degrees from³⁴, there is no ambiguity in the absolute rotation phase, and we were able to fit a quadratic polynomial to the measured rotation phase as a function of observation time (Eq. 5).

$$P = W_0 + W_1 T + W_2 T^2 \quad (5)$$

Since rotation rate is the time derivative of phase, W_1 is the rotation rate at $T = 0$ and $2W_2$ is the rate of change of the rotation rate. In Fig. 3, we plot this curve using $T = 0$ at the time of the first ground-based observation on 20 September 1999.

Code availability. This paper was produced using a number of different software packages. In some cases, versions of publicly available software were used with no custom modifications. This includes the software used for photometric reductions and manually inspection of images for dust and satellites (IRAF, <http://iraf.noao.edu/> and ds9, <http://ds9.si.edu/site/Home.html>).

We modified a version of the Comet Toolbox code (https://bitbucket.org/Once/comet_toolbox) to model potential dust trails from Benu³⁷. Dust mass and production rate spreadsheets are a straightforward implementation of the equations in³⁸. Versions of the dust trail, dust mass and production rates software and spreadsheets are available upon request to editors and reviewers.

The moving object detection software used by the Catalina Sky Survey is proprietary¹⁹. Two other methods were used to inspect images for satellites and other moving objects that involved no custom software and replicated and exceeded the capabilities of the Catalina Sky Survey software. The visual inspection of blinked images method defined the lower size limit of detectable satellites (Supplementary Table 1). The visual methods used the following two publicly available software packages: (IRAF, <http://iraf.noao.edu/> and ds9, <http://ds9.si.edu/site/Home.html>).

The Benu photometry was fitted with the Lommel-Seeliger, IAU H,G , and both the original²⁹ and the revised H,G_{12} phase function models³⁰. We used the implementation of the phase function models in the photometry module of the Python package for small-body planetary astronomy (sbpy) that is currently under development (<https://github.com/NASA-Planetary-Science/sbpy>)⁴⁶. The non-linear fitting of the revised H,G_{12} model was performed with the Levenberg-Marquardt algorithm⁴⁷ as implemented in the fitting module of astropy, which is a community-developed core Python package for astronomy⁴⁸.

Data availability

Raw through calibrated OCAMS images will be available via the Planetary Data System (PDS) (<https://sbn.psi.edu/pds/resource/orex/>). Data are delivered to the PDS according to the OSIRIS-REx Data Management Plan available in the OSIRIS-REx PDS archive. Higher-level products, such as co-added dust images, Benu photometry, and phase function model solutions, will be available in the Planetary Data System one year after departure from the asteroid. The source data underlying Figs. 3 and 4 are provided as a Source Data file. Source data for Fig. 2 is also contained in Supplementary Table 1 and for Fig. 3 in Supplementary Table 2.

The AAVSO Standard Field photometry for star cluster NGC 3532 can be found at https://www.aavso.org/apps/vsp/photometry/?east=right&fov=30.0&scale=E&north=down&orientation=visual&maglimit=16.5&resolution=1508ra=11%3A05%3A12.00&Rc=on&dec=-58%3A44%3A01.0&type=photometry&special=std_field&std_field=on. Calculations of distances and phase angles needed for mass loss rate determination is available to the public via JPL HORIZONS (<https://ssd.jpl.nasa.gov/?horizons>). Phase darkening coefficients for comments are available as of January 2019 from <http://asteroid.lowell.edu/comet/dustphase.html>.

Received: 31 January 2019 Accepted: 26 February 2019

Published online: 19 March 2019

References

- Lauretta, D. S. et al. OSIRIS-REx: sample return from asteroid (101955) Benu. *Space Sci. Rev.* **212**, 925–984 (2017).
- Rizk, B. et al. OCAMS: the OSIRIS-REx camera suite. *Space Sci. Rev.* **214**, 26 (2018).
- Hergenrother, C. W. et al. The design reference asteroid for the OSIRIS-REx Mission Target (101955) Benu. Preprint at <https://arxiv.org/abs/1409.4704> (2014).
- OSIRIS-REx, Mission Status Update, <https://www.asteroidmission.org/status-updates/>, (2019).
- Vokrouhlický, D., Bottke, W. F., Chesley, S. R., Scheeres, D. J., & Statler, T. S. in *Asteroids IV* (eds Michel, P., DeMeo, F. E., & Bottke, W. F.), 509–532 (University of Arizona Press, Tucson, AZ, 2015).
- Finson, M. J. & Probst, R. F. A theory of dust comets. I. Model and equations. *Astrophys. J.* **154**, 327–352 (1968).

7. Emery, J. P. et al. Thermal infrared observations and thermophysical characterization of OSIRIS-REx target asteroid (101955) Bennu. *Icarus* **234**, 17–35 (2014).
8. Snodgrass, C. et al. The Main Belt Comets and ice in the Solar System. *Astron. Astrophys. Rev.* **25**, 5 (2017).
9. Jewitt, D., Li, J. & Agarwal, J. The dust tail of asteroid (3200) Phaethon. *Astrophys. J. Lett.* **771**, L36 (2013).
10. DellaGiustina, D. N. et al. Properties of rubble-pile asteroid (101955) Bennu from OSIRIS-REx imaging and thermal analysis. *Nat. Astron.* <https://doi.org/10.1038/s41550-019-0731-1> (2019).
11. Walsh, K. J. et al. Craters, boulders and regolith of (101955) Bennu indicative of an old and dynamic surface. *Nat. Geosci.* <https://doi.org/10.1038/s41561-019-0326-6> (2019).
12. Marcus, J. N. Forward-scattering enhancement of comet brightness. I. Background and model. *Int. Comet Q.* **29**, 39–66 (2007).
13. Pravec, P. et al. Photometric survey of binary near-Earth asteroids. *Icarus* **181**, 63–93 (2006).
14. Johnston, W. R. Binary Minor Planets Compilation V2.0. NASA Planetary Data System (2018).
15. Scheeres, D. J. et al. The geophysical environment of Bennu. *Icarus* **276**, 116–140 (2016).
16. Rieger, S., Scheeres, D. J. & Barbee, B. Orbital Stability Regions for Hypothetical Natural Satellites of (101955) Bennu. *J. Spacecraft Rockets* <https://doi.org/10.2514/1.A34160> (2018).
17. Nolan, M. C. et al. Shape model and surface properties of the OSIRIS-REx target Asteroid (101955) Bennu from radar and lightcurve observations. *Icarus* **226**, 629–640 (2013).
18. Hergenrother, C. W. et al. Lightcurve, color and phase function photometry of the OSIRIS-REx target asteroid (101955) 1999 RQ36. *Icarus* **226**, 663–670 (2013).
19. Christensen, E. J. et al. Simulating the performance of ground-based optical asteroid surveys. *AAS DPS #46, Abstr. id.* **414**, 03 (2014).
20. Scheeres, D. J. et al. The dynamic geophysical environment of (101955) Bennu based on OSIRIS-REx measurements. *Nat. Astron.* <https://doi.org/10.1038/s41550-019-0721-3> (2019).
21. Fuse, T., Yoshida, F., Tholen, D., Ishiguro, M. & Saito, J. Searching satellites of asteroid Itokawa by imaging observation with Hayabusa spacecraft. *Earth Planets Space* **60**, 33–37 (2008).
22. Bertini, I. et al. Search for satellites near comet 67P/Churyumov-Gerasimenko using Rosetta/OSIRIS images. *Astron. Astrophys.* **583**, A19 (2015).
23. McFadden, L. A. et al. Vesta's missing moons: comprehensive search for natural satellites of Vesta by the Dawn spacecraft. *Icarus* **257**, 207–216 (2015).
24. McFadden, L. A. et al. Dawn mission's search for satellites of Ceres: intact protoplanets don't have satellites. *Icarus* **316**, 191–204 (2018).
25. Bos, B. et al. Touch And Go Camera System (TAGCAMS) for the OSIRIS-REx asteroid sample return mission. *Space Sci. Rev.* **214**, 37 (2018).
26. Belskaya, I. N. & Shevchenko, V. G. Opposition effect of asteroids. *Icarus* **147**, 94–105 (2000).
27. Hapke, B. *Theory of Reflectance and Emission Spectroscopy*. (Cambridge University Press, Cambridge, UK, 2012).
28. Bowell, E. et al. in *Asteroids II* (eds Binzel, R. P., Gehrels, T. G. & Matthews, M. A.), pp. 524–556, (University of Arizona Press, Tucson, AZ, 1989).
29. Muinonen, K. et al. A three-parameter magnitude phase function for asteroids. *Icarus* **209**, 542–555 (2010).
30. Penttilä, A., Shevchenko, V. G., Wilkman, O. & Muinonen, K. H, G1, G2 photometric phase function extended to low-accuracy data. *Planet. Space Sci.* **123**, 117–125 (2016).
31. Shevchenko, V. G. et al. Asteroid observations at low phase angles. *Bright. Behav. dark asteroids. Icarus* **196**, 601–611 (2008).
32. Li, J. Y., Helfenstein, P., Buratti, B., Takir, D. & Clark, B. E. (2015). in *Asteroids IV* (eds Michel, P., DeMeo, F. E., & Bottke, W. F.), 129–150 (University of Arizona Press, Tucson, AZ, 2015).
33. Shevchenko, V. G. & Belskaya, I. N. *Opposition effect of dark asteroids: Diversity and albedo dependence*. Abstr. for European Planetary Science Congress 2010, Rome, Italy, 738 (2010).
34. Nolan, M. C. et al. Detection of rotational acceleration of Bennu using HST lightcurve observations. *Geophys. Res. Lett.*, <https://doi.org/10.1029/2018GL080658> (2019).
35. Barnouin, O. S. et al. Shape of (101955) Bennu indicative of a rubble pile with internal stiffness. *Nat. Geosci.* <https://doi.org/10.1038/s41561-019-0330-x> (2019).
36. Durech, J. et al. YORP and Yarkovsky effects in asteroid (1685) Toro, (2100) Ra-Shalom, (3130) Eger, and (161989) Cacus. *Astron. Astrophys.* **609**, A86 (2018).
37. Vincent, J.-B. Comet-toolbox: numerical simulations of cometary dust tails in your browser. Asteroids Comets Meteors conference, Helsinki, (2014).
38. Jewitt, D. The active Centaurs. *Astron. J.* **137**, 4296–4312 (2009).
39. Schleicher, D. G., Millis, R. L. & Birch, P. V. Narrowband photometry of Comet P/Halley: variation with heliocentric distance, season, and solar phase angle. *Icarus* **132**, 397–417 (1998).
40. Grün, E. et al. (2010). Broadband infrared photometry of comet Hale-Bopp with ISOPHOT. *Astron. Astrophys.* **377**, 1098–1118 (2010).
41. Agarwal, J. et al. The dust trail of Comet 67P/Churyumov-Gerasimenko between 2004 and 2006. *Icarus* **207**, 992–1012 (2010).
42. Fulle, M. et al. Evolution of the dust size distribution of comet 67P/Churyumov-Gerasimenko from 2.2AU to perihelion. *Astrophys. J.* **821**, 19 (2016).
43. Hergenrother, C. W. et al. A search for Earth Trojan asteroids with the OSIRIS-REx spacecraft. *Lunar and Planetary Science Conference 2017*, Contribution No. 1964, id.2892 (2017).
44. Cambioni, S. et al. An upper limit on Earth's trojan asteroid population from OSIRIS-REx. *Lunar and Planetary Science Conference 2018*, Contribution No. 2083, id.1149 (2018).
45. Oszkiewicz, D. A. et al. Asteroid taxonomic signatures from photometric phase curve. *Icarus* **219**, 283–296 (2012).
46. NASA-Planetary Astronomy sbpy page, <https://github.com/NASA-Planetary-Science/sbpy>, (2019).
47. Marquardt, D. W. An algorithm for least-squares estimation of nonlinear parameter. *J. Soc. Ind. Appl. Math.* **11**, 431–441 (1963).
48. The Astropy Collaboration. et al. Astropy: a community Python package for astronomy. *Astron. Astrophys.* **558**, A33 (2013).
49. Lauretta, D. S. et al. The unexpected surface of asteroid (101955) Bennu. *Nature* <https://doi.org/10.1038/s41586-019-1033-6> (2019).
50. Magri, C. et al. Radar observations and a physical model of Asteroid 1580 Betulia. *Icarus* **186**, 152–177 (2007).

Acknowledgements

This material is based upon work supported by NASA under Contract NNM10AA11C issued through the New Frontiers Program. This work made use of sbpy (<http://sbpy.org>), a community-driven Python package for small-body planetary astronomy supported by NASA PDART Grant No. 80NSSC18K0987. A portion of this research was carried out at the Jet Propulsion Laboratory, California Institute of Technology, under a contract with the National Aeronautics and Space Administration. M.A.B. and S.F. acknowledge financial support from CNES. We thank Vishnu Reddy for useful suggestions to improve the manuscript.

Author contributions

C.W.H. is the head of the OSIRIS-REx Astronomy Working Group. He is responsible for the design and implementation of the Approach phase campaign and led the data reduction. C.K.M. is a member of the Astronomy Working Group and responsible for Finson-Probst analysis and estimating bounds on the dust trail mass loss rate. M.C.N. provided the lightcurve analysis and text for the manuscript in this section. J.-Y.L., B.E.C., and X.-D.Z. provided text and fitting of photometric models to our phase function data. C.D.d'A., D.N.D., D.R.G. and P.H.S. are responsible for calibration of the OCAMS instrument and related data reduction tasks. F.C.S. and E.J.C. analyzed the hazard search images for detections of natural satellites. T.R.K. assisted in data reduction of the phase function photometry. S.F., M.A.B., H.C., and M.R.M.I., provided insight and contributed text into comparing our results from Bennu to other spacecraft targets such as 67P and Ryugu. S.R.C. and D.J.S. were involved in the design of the hazards search. E.B.B., C.M.H., E.S.H., B.R. provided commentary and suggestions to the manuscript. D.S.L. leads the OSIRIS-REx mission and is responsible for the overall scientific investigation, the development and implementation of mission requirements, and leadership of the science and operations mission teams. He contributed substantially to the content of this manuscript. The OSIRIS-REx team is in charge of executing the OSIRIS-REx mission for NASA, and is responsible for producing data products from mission instruments that will be made available to the scientific community.

Additional information

Supplementary Information accompanies this paper at <https://doi.org/10.1038/s41467-019-09213-x>.

Competing interests: The authors declare no competing interests.

Reprints and permission information is available online at <http://npg.nature.com/reprintsandpermissions/>

Journal peer review information: *Nature Communications* thanks Vasilij Shevchenko, and the other anonymous reviewers for their contribution to the peer review of this work. Peer reviewer reports are available.

Publisher's note: Springer Nature remains neutral with regard to jurisdictional claims in published maps and institutional affiliations.



Open Access This article is licensed under a Creative Commons Attribution 4.0 International License, which permits use, sharing, adaptation, distribution and reproduction in any medium or format, as long as you give appropriate credit to the original author(s) and the source, provide a link to the Creative Commons license, and indicate if changes were made. The images or other third party material in this article are included in the article's Creative Commons license, unless indicated otherwise in a credit line to the material. If material is not included in the article's Creative Commons license and your intended use is not permitted by statutory regulation or exceeds the permitted use, you will need to obtain permission directly from the copyright holder. To view a copy of this license, visit <http://creativecommons.org/licenses/by/4.0/>.

© The Author(s) 2019

The OSIRIS-Rex Team

D.E. Highsmith¹¹, J. Small¹¹, D. Vokrouhlický¹², N.E. Bowles¹³, E. Brown¹³, K.L. Donaldson Hanna¹³, T. Warren¹³, C. Brunet¹⁴, R.A. Chicoine¹⁴, S. Desjardins¹⁴, D. Gaudreau¹⁴, T. Haltigin¹⁴, S. Millington-Veloza¹⁴, A. Rubi¹⁴, J. Aponte¹⁵, N. Gorius¹⁵, A. Lunsford¹⁵, B. Allen¹⁶, J. Grindlay¹⁶, D. Guevel¹⁶, D. Hoak¹⁶, J. Hong¹⁶, D.L. Schrader¹⁷, J. Bayron¹⁸, O. Golubov¹⁹, P. Sánchez¹⁹, J. Stromberg²⁰, M. Hirabayashi²¹, C.M. Hartzell⁹, S. Oliver²², M. Rascon²², A. Harch²³, J. Joseph²³, S. Squyres²³, D. Richardson²⁴, J.P. Emery²⁵, L. McGraw²⁵, R. Ghent²⁶, R.P. Binzel²⁷, M.M. Al Asad²⁸, C.L. Johnson^{2,28}, L. Philpott²⁸, H.C.M. Susorney²⁸, E.A. Cloutis²⁹, R.D. Hanna³⁰, H.C. Connolly Jr.³¹, F. Ciceri³², A.R. Hildebrand³², E.-M. Ibrahim³², L. Breitenfeld³³, T. Glotch³³, A.D. Rogers³³, B.E. Clark⁸, S. Ferrone⁸, C.A. Thomas³⁴, H. Campins⁶, Y. Fernandez⁶, W. Chang³⁵, A. Chevront³⁶, D. Trang³⁷, S. Tachibana³⁸, H. Yurimoto³⁸, J.R. Brucato³⁹, G. Poggiali³⁹, M. Pajola⁴⁰, E. Dotto⁴¹, E. Mazzotta Epifani⁴¹, M.K. Crombie⁴², C. Lantz⁴³, M.R.M. Izawa⁴⁴, J. de Leon⁴⁴, J. Licandro⁴⁴, J.L. Rizos Garcia⁴⁴, S. Clemett⁴⁵, K. Thomas-Keprta⁴⁵, S. Van wal⁴⁶, M. Yoshikawa⁴⁶, J. Bellerose⁷, S. Bhaskaran⁷, C. Boyles⁷, S.R. Chesley⁷, C.M. Elder⁷, D. Farnocchia⁷, A. Harbison⁷, B. Kennedy⁷, A. Knight⁷, N. Martinez-Vlasoff⁷, N. Mastrodemos⁷, T. McElrath⁷, W. Owen⁷, R. Park⁷, B. Rush⁷, L. Swanson⁷, Y. Takahashi⁷, D. Velez⁷, K. Yetter⁷, C. Thayer⁴⁷, C. Adam⁴⁸, P. Antreasian⁴⁸, J. Bauman⁴⁸, C. Bryan⁴⁸, B. Carcich⁴⁸, M. Corvin⁴⁸, J. Geeraert⁴⁸, J. Hoffman⁴⁸, J.M. Leonard⁴⁸, E. Lessac-Chenen⁴⁸, A. Levine⁴⁸, J. McAdams⁴⁸, L. McCarthy⁴⁸, D. Nelson⁴⁸, B. Page⁴⁸, J. Pelgrift⁴⁸, E. Sahr⁴⁸, K. Stakkestad⁴⁸, D. Stanbridge⁴⁸, D. Wibben⁴⁸, B. Williams⁴⁸, K. Williams⁴⁸, P. Wolff⁴⁸, P. Hayne⁴⁹, D. Kubitschek⁴⁹, M.A. Barucci⁴, J.D.P. Deshapriya⁴, S. Fornasier⁴, M. Fulchignoni⁴, P. Hasselmann⁴, F. Merlin⁴, A. Praet⁴, E.B. Bierhaus⁵, O. Billett⁵, A. Boggs⁵, B. Buck⁵, S. Carlson-Kelly⁵, J. Cerna⁵, K. Chaffin⁵, E. Church⁵, M. Coltrin⁵, J. Daly⁵, A. Deguzman⁵, R. Dubisher⁵, D. Eckart⁵, D. Ellis⁵, P. Falkenstein⁵, A. Fisher⁵, M.E. Fisher⁵, P. Fleming⁵, K. Fortney⁵, S. Francis⁵, S. Freund⁵, S. Gonzales⁵, P. Haas⁵, A. Hasten⁵, D. Hauf⁵, A. Hilbert⁵, D. Howell⁵, F. Jaen⁵, N. Jayakody⁵, M. Jenkins⁵, K. Johnson⁵, M. Lefevre⁵, H. Ma⁵, C. Mario⁵, K. Martin⁵, C. May⁵, M. McGee⁵, B. Miller⁵, C. Miller⁵, G. Miller⁵, A. Mirfakhrai⁵, E. Muhle⁵, C. Norman⁵, R. Olds⁵, C. Parish⁵, M. Ryle⁵, M. Schmitzer⁵, P. Sherman⁵, M. Skeen⁵, M. Susak⁵, B. Sutter⁵, Q. Tran⁵, C. Welch⁵, R. Witherspoon⁵, J. Wood⁵, J. Zareski⁵, M. Arvizu-Jakubicki¹, E. Asphaug¹, E. Audi¹, R.-L. Ballouz¹, R. Bandrowski¹, K.J. Becker¹, T.L. Becker¹, S. Bendall¹, C.A. Bennett¹, H. Bloomenthal¹, D. Blum¹, W.V. Boynton¹, J. Brodbeck¹, K.N. Burke¹, M. Chojnacki¹, A. Colpo¹, J. Contreras¹, J. Cutts¹, C.Y. Drouet d'Aubigny¹, D. Dean¹, D.N. DellaGiustina¹, B. Diallo¹, D. Drinnon¹, K. Drozd¹, H.L. Enos¹, R. Enos¹, C. Fellows¹, T. Ferro¹, M.R. Fisher¹, G. Fitzgibbon¹, M. Fitzgibbon¹, J. Forelli¹, T. Forrester¹, I. Galinsky¹, R. Garcia¹, A. Gardner¹, D.R. Golish¹, N. Habib¹, D. Hamara¹, D. Hammond¹, K. Hanley¹, K. Harshman¹, C.W. Hergenrother¹, K. Herzog¹, D. Hill¹, C. Hoekenga¹, S. Hooven¹, E.S. Howell¹, E. Huettnner¹, A. Janakus¹, J. Jones¹, T.R. Kareta¹, J. Kidd¹, K. Kingsbury¹, S.S. Balram-Knutson¹, L. Koelbel¹, J. Kreiner¹, D. Lambert¹, D.S. Lauretta¹, C. Lewin¹, B. Lovelace¹, M. Loveridge¹, M. Lujan¹, C.K. Maleszewski¹, R. Malhotra¹, K. Marchese¹, E. McDonough¹, N. Mogk¹, V. Morrison¹, E. Morton¹,

R. Munoz¹, J. Nelson¹, M.C. Nolan¹, J. Padilla¹, R. Pennington¹, A. Polit¹, N. Ramos¹, V. Reddy¹, M. Riehl¹, B. Rizk¹, H.L. Roper¹, S. Salazar¹, S.R. Schwartz¹, S. Selznick¹, N. Shultz¹, P.H. Smith¹, S. Stewart¹, S. Sutton¹, T. Swindle¹, Y.H. Tang¹, M. Westermann¹, C.W.V. Wolner¹, D. Worden¹, T. Zega¹, Z. Zeszut¹, A. Bjurström⁵⁰, L. Bloomquist⁵⁰, C. Dickinson⁵⁰, E. Keates⁵⁰, J. Liang⁵⁰, V. Nifo⁵⁰, A. Taylor⁵⁰, F. Teti⁵⁰, M. Caplinger⁵¹, H. Bowles⁵², S. Carter⁵², S. Dickenshied⁵², D. Doerres⁵², T. Fisher⁵², W. Hagee⁵², J. Hill⁵², M. Miner⁵², D. Noss⁵², N. Piacentine⁵², M. Smith⁵², A. Toland⁵², P. Wren⁵², M. Bernacki⁵³, D. Pino Munoz⁵³, S.-i. Watanabe^{46,54}, S.A. Sandford⁵⁵, A. Aqueche⁵⁶, B. Ashman⁵⁶, M. Barker⁵⁶, A. Bartels⁵⁶, K. Berry⁵⁶, B. Bos⁵⁶, R. Burns⁵⁶, A. Calloway⁵⁶, R. Carpenter⁵⁶, N. Castro⁵⁶, R. Cosentino⁵⁶, J. Donaldson⁵⁶, J.P. Dworkin⁵⁶, J. Elsila Cook⁵⁶, C. Emr⁵⁶, D. Everett⁵⁶, D. Fennell⁵⁶, K. Fleshman⁵⁶, D. Folta⁵⁶, D. Gallagher⁵⁶, J. Garvin⁵⁶, K. Getzandanner⁵⁶, D. Glavin⁵⁶, S. Hull⁵⁶, K. Hyde⁵⁶, H. Ido⁵⁶, A. Ingegneri⁵⁶, N. Jones⁵⁶, P. Kaotira⁵⁶, L.F. Lim⁵⁶, A. Liounis⁵⁶, C. Lorentson⁵⁶, D. Lorenz⁵⁶, J. Lyzhoft⁵⁶, E.M. Mazarico⁵⁶, R. Mink⁵⁶, W. Moore⁵⁶, M. Moreau⁵⁶, S. Mullen⁵⁶, J. Nagy⁵⁶, G. Neumann⁵⁶, J. Nuth⁵⁶, D. Poland⁵⁶, D.C. Reuter⁵⁶, L. Rhoads⁵⁶, S. Rieger⁵⁶, D. Rowlands⁵⁶, D. Sallitt⁵⁶, A. Scroggins⁵⁶, G. Shaw⁵⁶, A.A. Simon⁵⁶, J. Swenson⁵⁶, P. Vasudeva⁵⁶, M. Wasser⁵⁶, R. Zellar⁵⁶, J. Grossman⁵⁷, G. Johnston⁵⁷, M. Morris⁵⁷, J. Wendel⁵⁷, A. Burton⁵⁸, L.P. Keller⁵⁸, L. McNamara⁵⁸, S. Messenger⁵⁸, K. Nakamura-Messenger⁵⁸, A. Nguyen⁵⁸, K. Righter⁵⁸, E. Queen⁵⁹, K. Bellamy⁶⁰, K. Dill⁶⁰, S. Gardner⁶⁰, M. Giuntini⁶⁰, B. Key⁶⁰, J. Kissell⁶⁰, D. Patterson⁶⁰, D. Vaughan⁶⁰, B. Wright⁶⁰, R.W. Gaskell², L. Le Corre², J.-Y. Li², J.L. Molaro², E.E. Palmer², M.A. Siegler², P. Tricarico², J.R. Weirich², X.-D. Zou², T. Ireland⁶¹, K. Tait⁶², P. Bland⁶³, S. Anwar⁶⁴, N. Bojorquez-Murphy⁶⁴, P.R. Christensen⁶⁴, C.W. Haberle⁶⁴, G. Mehall⁶⁴, K. Rios⁶⁴, I. Franchi⁶⁵, B. Rozitis⁶⁵, C.B. Beddingfield⁶⁶, J. Marshall⁶⁶, D.N. Brack¹⁰, A.S. French¹⁰, J.W. McMahon¹⁰, D.J. Scheeres¹⁰, E.R. Jawin⁶⁷, T.J. McCoy⁶⁷, S. Russell⁶⁷, M. Killgore⁶⁸, W.F. Bottke⁶⁹, V.E. Hamilton⁶⁹, H.H. Kaplan⁶⁹, K.J. Walsh⁶⁹, J.L. Bandfield⁷⁰, B.C. Clark⁷⁰, M. Chodas⁷¹, M. Lambert⁷¹, R.A. Masterson⁷¹, M.G. Daly⁷², J. Freemantle⁷², J.A. Seabrook⁷², O.S. Barnouin⁷³, K. Craft⁷³, R.T. Daly⁷³, C. Ernst⁷³, R.C. Espiritu⁷³, M. Holdridge⁷³, M. Jones⁷³, A.H. Nair⁷³, L. Nguyen⁷³, J. Peachey⁷³, M.E. Perry⁷³, J. Plescia⁷³, J.H. Roberts⁷³, R. Steele⁷³, R. Turner⁷³, J. Backer⁷⁴, K. Edmundson⁷⁴, J. Mapel⁷⁴, M. Milazzo⁷⁴, S. Sides⁷⁴, C. Manzoni⁷⁵, B. May⁷⁵, M. Delbo⁷⁶, G. Libourel⁷⁶, P. Michel⁷⁶, A. Ryan⁷⁶, F. Thuillet⁷⁶ & B. Marty⁷⁷

¹¹Aerospace Corporation, Chantilly, VA, USA. ¹²Astronomical Institute, Charles University, Prague, Czech Republic. ¹³Atmospheric, Oceanic and Planetary Physics, University of Oxford, Oxford, UK. ¹⁴Canadian Space Agency, Saint-Hubert, Quebec, Canada. ¹⁵Catholic University of America, Washington, DC, USA. ¹⁶Center for Astrophysics, Harvard University, Cambridge, MA, USA. ¹⁷Center for Meteorite Studies, Arizona State University, Tempe, AZ, USA. ¹⁸City University of New York, New York, NY, USA. ¹⁹Colorado Center for Astrodynamics Research, University of Colorado, Boulder, CO, USA. ²⁰Commonwealth Scientific and Industrial Research Organisation (CSIRO), Canberra, Australian Capital Territory, Australia. ²¹Department of Aerospace Engineering, Auburn University, Auburn, AL, USA. ²²Department of Astronomy and Steward Observatory, University of Arizona, Tucson, AZ, USA. ²³Department of Astronomy, Cornell University, Ithaca, NY, USA. ²⁴Department of Astronomy, University of Maryland, College Park, MD, USA. ²⁵Department of Earth and Planetary Sciences, University of Tennessee, Knoxville, TN, USA. ²⁶Department of Earth Sciences, University of Toronto, Toronto, Ontario, Canada. ²⁷Department of Earth, Atmospheric, and Planetary Sciences, Massachusetts Institute of Technology, Cambridge, MA, USA. ²⁸Present address: Department of Earth, Ocean and Atmospheric Sciences, University of British Columbia, Vancouver, British Columbia, Canada. ²⁹Department of Geography, University of Winnipeg, Winnipeg, Manitoba, Canada. ³⁰Department of Geological Sciences, Jackson School of Geosciences, University of Texas, Austin, TX, USA. ³¹Department of Geology, Rowan University, Glassboro, NJ, USA. ³²Department of Geoscience, University of Calgary, Calgary, Alberta, Canada. ³³Department of Geosciences, Stony Brook University, Stony Brook, NY, USA. ³⁴Department of Physics and Astronomy, Northern Arizona University, Flagstaff, AZ, USA. ³⁵Edge Space Systems, Greenbelt, MD, USA. ³⁶General Dynamics C4 Systems, Denver, CO, USA. ³⁷Hawai'i Institute of Geophysics and Planetology, University of Hawai'i at Mānoa, Honolulu, HI, USA. ³⁸Hokkaido University, Sapporo, Japan. ³⁹INAF—Astrophysical Observatory of Arcetri, Florence, Italy. ⁴⁰INAF—Osservatorio Astronomico di Padova, Padova, Italy. ⁴¹INAF—Osservatorio Astronomico di Roma, Rome, Italy. ⁴²Indigo Information Services, Tucson, AZ, USA. ⁴³Institut d'Astrophysique Spatiale, CNRS/Université Paris Sud, Orsay, France. ⁴⁴Instituto de Astrofísica de Canarias and Departamento de Astrofísica, Universidad de La Laguna, Tenerife, Spain. ⁴⁵Jacobs Technology, Houston, TX, USA. ⁴⁶JAXA Institute of Space and Astronautical Science, Sagami, Japan. ⁴⁷Kavli Institute for Astrophysics and Space Research, Massachusetts Institute of Technology, Cambridge, MA, USA. ⁴⁸KinetX Aerospace, Inc., Simi Valley, CA, USA. ⁴⁹Laboratory for Atmospheric and Space Physics, University of Colorado, Boulder, CO, USA. ⁵⁰Macdonald, Dettwiler, and Associates, Brampton, Ontario, Canada. ⁵¹Malin Space Science Systems, San Diego, CA, USA. ⁵²Mars Space Flight Facility, Arizona State University, Tempe, AZ, USA. ⁵³Mines ParisTech, Paris, France. ⁵⁴Nagoya University, Nagoya, Japan. ⁵⁵NASA Ames Research Center, Moffett Field, CA, USA. ⁵⁶NASA Goddard Space Flight Center, Greenbelt, MD, USA. ⁵⁷NASA Headquarters, Washington, DC, USA. ⁵⁸NASA Johnson Space Center, Houston, TX, USA. ⁵⁹NASA Langley Research Center, Hampton, VA, USA. ⁶⁰NASA Marshall Space Flight Center, Huntsville, AL, USA. ⁶¹Research School of Earth Sciences, Australian National University, Canberra, Australian Capital Territory, Australia. ⁶²Royal Ontario Museum, Toronto, Ontario, Canada. ⁶³School of Earth and Planetary Sciences, Curtin University, Perth, Western Australia, Australia. ⁶⁴School of Earth and Space Exploration, Arizona State University, Tempe, AZ, USA. ⁶⁵School of Physical Sciences, The Open

University, Milton Keynes, UK. ⁶⁶SETI Institute, Mountain View, CA, USA. ⁶⁷Smithsonian Institution National Museum of Natural History, Washington, DC, USA. ⁶⁸Southwest Meteorite Laboratory, Payson, AZ, USA. ⁶⁹Southwest Research Institute, Boulder, CO, USA. ⁷⁰Space Science Institute, Boulder, CO, USA. ⁷¹Space Systems Laboratory, Department of Aeronautics and Astronautics, Massachusetts Institute of Technology, Cambridge, MA, USA. ⁷²The Centre for Research in Earth and Space Science, York University, Toronto, Ontario, Canada. ⁷³The Johns Hopkins University Applied Physics Laboratory, Laurel, MD, USA. ⁷⁴U.S. Geological Survey Astrogeology Science Center, Flagstaff, AZ, USA. ⁷⁵London Stereoscopic Company, London, UK. ⁷⁶Université Côte d'Azur, Observatoire de la Côte d'Azur, CNRS, Laboratoire Lagrange, Nice, France. ⁷⁷Université de Lorraine, Nancy, France